A Microscale Model of Bacterial and Biofilm Dynamics in Porous Media

Robert Dillon,[1] Lisa Fauci[2]

[1]Department of Pure and Applied Mathematics, Washington State University, Pullman, Washington 99164; telephone: 509-335-5110; fax: 509-335-1188; e-mail: dillon@math.wsu.edu
[2]Department of Mathematics, Tulane University, New Orleans, Louisiana

Received 3 July 1999; accepted 19 December 1999

Abstract: A microscale model for the transport and coupled reaction of microbes and chemicals in an idealized two-dimensional porous media has been developed. This model includes the flow, transport, and bioreaction of nutrients, electron acceptors, and microbial cells in a saturated granular porous media. The fluid and chemicals are represented as a continuum, but the bacterial cells and solid granular particles are represented discretely. Bacterial cells can attach to the particle surfaces or be advected in the bulk fluid. The bacterial cells can also be motile and move preferentially via a run and tumble mechanism toward a chemoattractant. The bacteria consume oxygen and nutrients and alter the profiles of these chemicals. Attachment of bacterial cells to the soil matrix and growth of bacteria can change the local permeability. The coupling of mass transport and bioreaction can produce spatial gradients of nutrients and electron acceptor concentrations. We describe a numerical method for the microscale model, show results of a convergence study, and present example simulations of the model system. *Biotechnol Bioeng* **68:** 536–547, 2000.
Keywords: porous media; biofilm model; immersed boundary method; mass transport; bioremediation

INTRODUCTION

Microbial processes in saturated groundwater systems are of relevance in a variety of areas including oil recovery, oil souring, the transport of pathogens in groundwater systems, and the transport of contaminants by microbes. Microbial degradation of organic chemicals is widely regarded as one of the primary strategies available for remediation of contaminated soils and groundwater systems. Microbial communities are often found in these contaminated systems even at great depths. In situ bioremediation strategies attempt to enhance the natural biodegradation rates by injecting nutrients into the subsurface to stimulate the bacterial population growth. The success of this strategy depends on the mechanisms governing the transport of fluid and chemicals within the porous media, the growth and movement of bacteria within the subsurface of the microenvironment.

An important aspect of microbial processes is the propensity of cells to adhere and bind to a surface. The adsorbed cells produce a matrix of polysaccharide fibers binding the cells to the surface and to other cells. The structure associated with biofilms (cf. Bishop, 1997) may be very different in porous media where the term "bioweb" has been employed (Paulsen et al., 1997). Biofilm forms an essential part of the porous media—altering its microscale geometry and chemical environment. At the same time, substrates are transported from the bulk fluid to the biofilm by diffusion and advection processes and are consumed by the cells. Substrates may also be embedded within the soil matrix itself and diffuse into the bulk fluid or into the biofilm. The Pseudomonas family of bacteria are important in the context of bioremediation because of their ability to consume a variety of organic toxins. Many of these bacteria live as motile organisms in the bulk fluid or as sessile organisms attached to a surface. Thus, the distribution of bacterial populations may depend on active bacterial motility, passive transport via fluid advection, and population expansion through cell division.

Mathematical models addressing biofilm processes have been developed for saturated soils and aquifers (Baveye and Valocchi, 1989) and closed conduits (Szego et al., 1993). Field-scale models addressing geochemical and microbiological reactions on the field-scale level have been proposed (for example, see Tebes-Stevens et al., 1998). A two-dimensional model of microscale transport and biotransformation that couples the Navier–Stokes equations, advection and diffusion of a nonreacting chemical substrate, as well as cell–cell and cell-substratum adhesion was presented in Chen et al. (1994). Cellular automata models of biofilm development have been described in (Hermanowicz, 1997; Picioreanu et al., 1998; Wimpenny and Colasanti, 1997).

The microscale model described in this article is an extension of an earlier model of biofilm processes developed in part by the authors and described in Dillon et al. (1995, 1996). The earlier model was restricted to microchannel geometries and included the motility and chemotaxis of bacteria, the attachment and detachment of bacteria to the chan-

Correspondence to: R. Dillon
Contract grant sponsors: NSF Postdoctural Research Fellowship; National Science Foundation; NSF grant; NSF Group Infrastructure Grant
Contract grant numbers: DMS-9508815; DMS-9805501; DMS 9805492; DMS 9709754

nel walls and other bacteria as well as the transport and consumption of a nutrient or contaminant. Here, the microchannel is replaced with an idealized two-dimensional representation of porous media. The extension to a more complex geometry required significant changes in the numerical algorithms and can be used to study a variety of issues in the porous-media microenvironment. In the following, we give a general overview of the model and a mathematical description of its several components. In addition, we describe the numerical algorithm, report the results of convergence studies, and show several sample numerical simulations of the full-model system.

MATHEMATICAL MODEL

General Background

Biofilm formation in porous media is a complex, dynamic process. In this model, the coupling of fluid mechanics to chemical transport, microbial motility, chemotactic responses, and cell attachment is explicitly included. In addition, cells may be removed from the biofilm by flow properties that lead to detachment, such as shear stress. The dynamic evolution of biofilm shape changes the geometry of the porous media, and thus alters the fluid dynamics. The equations of motion for the fluid, microbes, porous structure, and chemicals will be presented below.

The model (a schematic of which is shown in Fig. 1) includes the following components:

- *The porous media idealized as a two-dimensional array of cylinders within a fluid section.* It is not required for the cylinders to be of uniform shape, size, or distribution. Although the solid phase could be modeled as a finer-scale porous media, the cylindrical particles are assumed to be solid.
- *A population of discrete bacterial cells.* Some may be attached to the surfaces and others may be in a planktonic state freely swimming within the fluid pores. The swimming cells may attach to the surfaces or to other cells. In addition, cells may detach from the surfaces. We do not present the trajectories of the microbes, rather, these are determined by the coupled equations of motion.
- *A background flow of fluid through the section due to the flow of groundwater*. We assume that the fluid flow through the section is governed by the Navier–Stokes equations for a viscous, incompressible fluid. The geometry of the fluid domain can change due to bacterial cells attaching and detaching from the solid phase. In addition, the swimming forces applied by the motile bacteria also influence the fluid flow.
- *A hydrocarbon substrate and an electron acceptor (i.e., oxygen).* These chemicals may be found either within the bulk fluid or the solid matrix. They are transported by advection and diffusion within the fluid and may be consumed by the bacteria. The biochemical reactions occur only at the sites of the bacterial cells.
- *Chemotactic response.* The swimming direction of the motile bacteria may be determined in part by an underlying chemoattractant. In particular, a stochastic, run-and-tumble strategy is implemented.

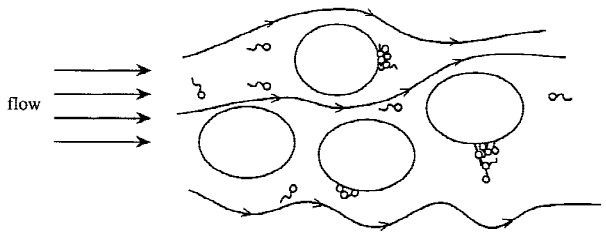

Figure 1. Schematic of saturated porous media with solid particles, fluid, and bacterial cells.

In Figure 2a we show a fluid-velocity field, particle, and microbe positions from a representative calculation. This

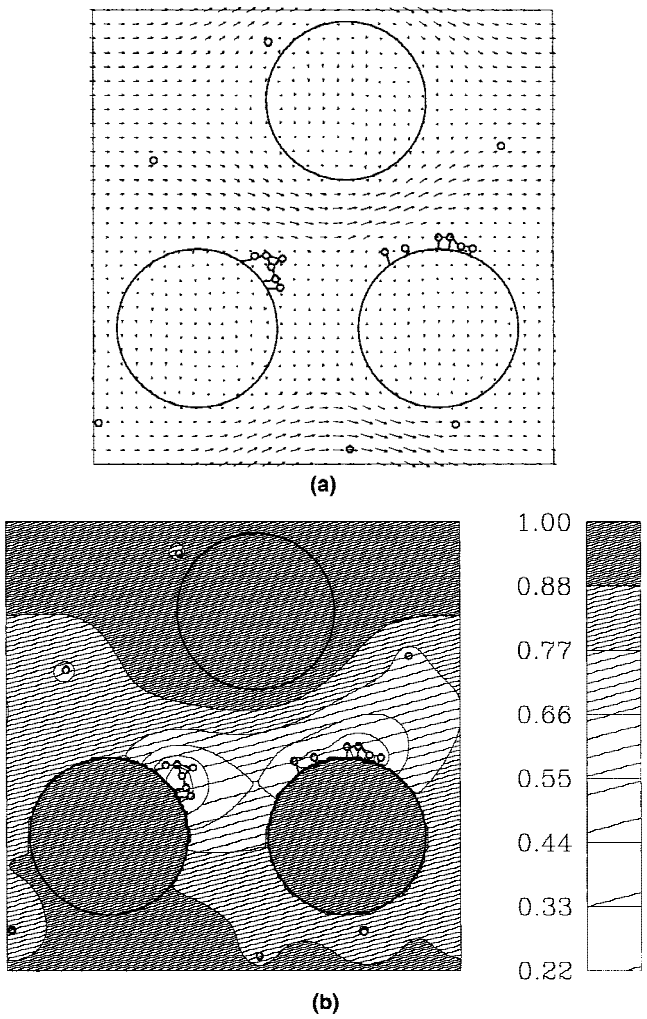

Figure 2. Velocity field (a) and chemical field (b) from a model simulation. The maximum speed depicted in the fluid velocity field is approximately 500 μm s^{-1}. The chemical concentrations shown are in nondimensional units. Unless otherwise indicated, the label bar shown here applies to all figures.

snapshot shows that some cells are freely swimming, while others have formed microcolonies attached to the solid particles. Figure 2b depicts contours of a nutrient-concentration field. Note the depletion of this nutrient near the microbe sites due to consumption. A detailed description of similar numerical descriptions is shown later in this article.

In the microscale model, characteristic time scales for growth processes are much longer than characteristic time scales for fluid advection and chemical diffusion. Typical doubling times for bacteria in a natural environment are on the order of hours. A typical bulk-fluid-flow rate U in a porous media is 1 meter per day or equivalently, 11.6 μm s^{-1}. For characteristic length scales L of 10 μm, a characteristic time scale for advection processes is $L/U \approx 1$ s. For diffusion rates on the order of $D \approx 10^{-5}$ cm^2 s^{-1}, a characteristic time scale for chemical diffusion is $L^2/D \approx 0.1$ s. Because the growth time scales are much longer than the fluid advection and diffusion time scales, we can ignore growth in these simulations.

Given the above characteristic length scale $L \approx 10$ μm, the kinematic viscosity of water $\nu \approx 0.01$ cm^2 s^{-1} and characteristic velocity scales U in the range of (1, 1000)μm s^{-1}, the Reynolds numbers $R_e = LU/\nu$ associated with the microscale are small (10^{-4}, 10^{-1}). The Péclet numbers $P_e = LU/D$ based on the characteristic length, velocity and diffusivities given above are in the range of (10^{-2}, 10). Thus, there is a transition from diffusion dominated transport processes to advection dominated processes depending upon the velocity U.

Mathematical Model

We present a system of coupled nonlinear equations which describes a microscale-porous media system. The mathematical framework and numerical method is based in part on the immersed boundary method. This method was introduced by Peskin (1977) to model blood flow in the heart and has subsequently been used in a variety of applications including the study of aquatic locomotion (Fauci and Peskin, 1988), platelet aggregation (Fogelson, 1984), three-dimensional blood flow in the heart (Peskin and McQueen, 1989a, 1989b), vertebrate limb development (Dillon and Othmer, 1999), large deformation of red blood cells (Eggleton and Popel, 1998), as well as fluid flow and mass transport in arterioles (Arthurs et al., 1998).

We assume that the fluid dynamics are governed by the Navier–Stokes equations:

$$\rho(\mathbf{u}_t + (\mathbf{u} \cdot \nabla)\mathbf{u}) = -\nabla p + \mu\nabla^2\mathbf{u} + \mathbf{F}, \tag{1}$$

$$\nabla \cdot \mathbf{u} = 0. \tag{2}$$

These equations describe the balance of momentum and conservation of mass in a viscous incompressible fluid. Here ρ is the fluid density, $\mathbf{u}$ is the fluid velocity vector, p is pressure, and μ is the fluid viscosity. The term $\mathbf{F}$ is the force density (force per unit area in two dimensions) that the microbes and the boundaries of the solid particles exert on the fluid:

$$\mathbf{F} = \sum_i \mathbf{F}_{cell(i)} + \mathbf{F}_{swim(i)} + \sum_j \mathbf{F}_{particle(j)} + \sum_{i,k} \mathbf{F}_{cc(i,k)} + \sum_{i,j} \mathbf{F}_{cp(i,j)} + \mathbf{F}_{drive} \tag{3}$$

Here $i, k = 1, \ldots, N_c$, where N_c is the number of bacterial cells and $j = 1, \ldots, N_p$, where N_p is the number of solid particles within the porous media array. The contributions to the force density given in Eq. (3) will be discussed below.

The bacterial cell body of each microorganism is modeled (in two dimensions) as an elastic ring, whose configuration is defined by the function $\mathbf{X}_i(s, t)$, where s is a Lagrangian label (e.g., arc length with respect to an equilibrium configuration), t is time and i denotes the i^{th} microbe. The boundary force per unit length $\mathbf{f}_{\mathbf{cell}(i)}(s, t)$ at each point on the ring consists of a tangential elastic-spring force and a normal bending-resistant force. These are designed to preserve the size and the shape, respectively, of the ring. In our simulations, the stiffness constants associated with the cell ring are chosen to reflect the stiffness properties of a bacterial cell wall. This "immersed boundary force" is transmitted directly to the fluid and gives a contribution to $\mathbf{F}$ which we call $\mathbf{F}_{\mathbf{cell}(i)}$:

$$\mathbf{F}_{\mathbf{cell}(i)}(\mathbf{x},t) = \int_{microbe} \mathbf{f}_{\mathbf{cell}(i)}(s,t)\delta(\mathbf{x} - \mathbf{X}_i(s,t))ds. \tag{4}$$

Here, the integration is over the points of the ring and δ is the two-dimensional Dirac delta function.

Bacterial motility is modeled in a simplified manner by means of a discrete set of forces applied to the fluid at points behind the cell body. These point forces are designed to represent the flagellar forces of a swimming bacteria. A detailed description of this mechanism as well as an algorithm for simulating the sequence of runs and tumbles characteristic of bacterial motility is presented in Dillon et al. (1995).

The boundaries of the solid particles are modeled in a manner similar to the microbe rings, that is, as neutrally buoyant elastic rings immersed within the fluid. However, these particles cannot move freely because they are also tethered to fixed points in space by stiff elastic springs:

$$\mathbf{f}_{particle(j)}(s,t) = -S_{tether}(\mathbf{X}_j(s,t) - \mathbf{X}_j^*(s)) \tag{5}$$

Here $\mathbf{X}_j(s,t)$ is the configuration of the j^{th} particle boundary, $\mathbf{X}_j^*(s)$ is the desired configuration of this particle boundary, and S_{tether} is the stiffness constant of this elastic force. Of course, this stiffness constant is chosen to be very large to keep the particle configuration fixed. We note that this representation of the soil matrix makes it easy to change the geometry of the pores simply by changing $\mathbf{X}_j^*(s)$. The large elastic boundary force given in Eq. (5) is transmitted to the fluid domain in a manner analogous to Eq. (4).

Microbial cell–cell or cell–particle adhesions are modeled by the creation of elastic springs of 'links' between points on each of the adherent entities. The model for link

formation is similar to the model for platelet adhesion and aggregation described in Fogelson (1984) and Fauci and Fogelson (1993). If the distance between the centroids of any given pair of cells is less than a prescribed cohesion distance, an elastic spring may be created to link the two cells. The mechanical properties of each spring and the cohesion distance are chosen to reflect biological and physicochemical properties of the system. The forces due to these springs are spread to the fluid domain and appear in Eq. (3) in the term $\mathbf{F}_{cc}$. Cell-particle links are formed in a similar manner ($\mathbf{F}_{cp}$). Detachment of cells from the biofilm is modeled by allowing the links to break when they are stretched beyond a prescribed length. Thus, the force term F in Eq. (3) includes several contributions arising from the cell bodies, solid-particle walls, cell–cell, and cell-substratum adhesion, and cell motility.

In our simulations, the fluid motion is driven by the force term force $\mathbf{F}_{drive}$ in Eq. (3). This applied force is constant in the horizontal direction and is equivalent to a uniform pressure gradient in the absence of any immersed obstacles and bacteria.

The immersed boundaries (microbes and solid particles) influence the fluid motion through the forces we have just described. In turn, the fluid motion and continuity of the fluid velocity field give equations of motion for the points $\mathbf{X}(s,t)$ on the immersed boundaries, namely:

$$\frac{d\mathbf{X}(s,t)}{dt} = \mathbf{u}(\mathbf{X}(s,t),t) = \int \mathbf{u}(\mathbf{x},t)\delta(\mathbf{x} - \mathbf{X}(s,t))d\mathbf{x}. \qquad (6)$$

Here the integration is over the entire domain. This can be interpreted as the usual no-slip boundary condition at a fluid–material interface.

The presence of microorganisms in the bulk fluid influences both the flow dynamics and chemical fields. The equations which describe the advection, diffusion, and consumption of the hydrocarbon substrate and the electron acceptor (oxygen) within the fluid-filled pore are:

$$s_t + (\mathbf{u} \cdot \nabla)s = D_s\nabla^2 s - R_s(s,a) \sum_{i=1}^{N_c} \delta(\overline{\mathbf{X}}_i - \mathbf{x}) \qquad (7)$$

$$a_t + (\mathbf{u} \cdot \nabla)a = D_a\nabla^2 a - R_a(s,a) \sum_{i=1}^{N_c} \delta(\overline{\mathbf{X}}_i - \mathbf{x}) \qquad (8)$$

where s is the hydrocarbon substrate concentration, D_s is its molecular diffusivity, a is the oxygen concentration, D_a its molecular diffusivity, and R_s and R_a are consumption rates. These are multiplied by the sum of Dirac delta functions centered at the centroid $\overline{\mathbf{X}}_i$ of the i^{th} microbe. This demonstrates that the consumption is nonzero only near the site of each of the N_c microbes (Dillon et al., 1995). While the microbe cells act as localized sinks of the chemical concentrations, the chemicals are free to diffuse through the microbial rings.

The no-slip, zero-velocity, boundary conditions for the fluid at the fluid–solid interfaces are enforced by means of Eqs. (5) and (6). The chemistry boundary conditions at these particle-fluid interfaces, unlike at the microbial rings, will be specified. We allow for two types of boundary conditions at the particle-fluid interface. We specify either a zero-flux Neumann boundary at the interface or a Dirichlet boundary condition in which the concentration level is fixed at the interface. The boundary conditions can vary from chemical species to chemical species and from interface to interface. In addition, a boundary condition for the chemicals on the computational fluid domain boundary must also be specified. We shall describe these domain boundary conditions in the section on computer simulations.

NUMERICAL METHODS

For computations, the fluid domain is discretized using a uniform rectangular grid, and the fluid variables (**u,** p, and **F**) and chemical concentrations (s and a) are defined on this grid. Similarly, the i^{th} immersed boundary is represented by a finite number of discrete Lagrangian points $\mathbf{X}_i$. The immersed boundary forces $\mathbf{f}_i$ are defined at these points. The immersed boundary points in general do not coincide with points of the fluid grid and communication between the immersed boundary points and the fluid grid is handled by a discretized version of the δ-function which appears in Eqs. (4), (6), (7), and (8). The discrete δ-function δ_h is given below.

The algorithm for the numerical solution of the coupled fluid–microbe–chemical system may be summarized as follows: At the beginning of each time step n, we have the fluid velocity field $\mathbf{u}^n$, the locations $\mathbf{X}_i^n$ of the immersed boundary points, the current configuration of the elastic links which connect these points, and the chemical concentration fields s^n and a^n. To update these values to reflect events that take place during this time step we:

1. Calculate the elastic force density $\mathbf{f}^n_{\mathbf{cell(i)}}$ or $\mathbf{f}^n_{\mathbf{particle(j)}}$ for each immersed boundary.
2. Calculate the swimming forces generated by each motile organism. These forces may be functions of the chemical-concentration fields.
3. Calculate the cell–cell and cell-particle link forces.
4. Spread all of these forces to the grid to determine the force density **F** which drives the fluid motion.
5. Solve the Navier–Stokes Eqs. (1)–(2) for $\mathbf{u}^{n+1}$.
6. Interpolate the fluid-velocity field to each immersed boundary point and move that point at its local fluid velocity [Eq. (6)] to determine $\mathbf{X}_i^{n+1}$.
7. Use the new positions of the microbes and alter the substrate concentration in the vicinity of each microbe to account for the consumption of substrate and solve the advection-diffusion-reaction equation for s^{n+1} and a^{n+1} (Eqs. (7)–(8)).

A constant force $\mathbf{F}_{drive}$ is added at each grid point to the force density **F** in step 4. For step 5, we use the projection method of Chorin (1968) with periodic boundary conditions. The discrete δ used in steps 4, 6, and 7 is defined by $\delta_h(\mathbf{x}) = d(x)d(y)$ where h is mesh width and

$$d(r) = \begin{cases} \frac{1}{4h}\left(1 + \cos\frac{\pi r}{2h}\right) & |r| < 2\,h \\ 0 & |r| \geq 2\,h. \end{cases} \quad (9)$$

See Peskin (1977) for details about δ_h.

The run-and-tumble process which influences the swimming forces calculated in Step 2 is implemented as follows: At discrete times, $t_j = t_{j-1} + \Delta t$, the chemoattractant concentration $S_k(t_j)$ at the k^{th} cell's centroid is determined. The tumbling probabilities are assumed to be exponentially distributed. If $S_k(t_j) > S_k(t_{j-1})$, we set the tumbling frequency $\lambda_k = \Lambda_0$; otherwise, $\lambda_k = \Lambda_1$. The values of Λ_0 and Λ_1 determine the chemotactic sensitivity of the microbes. See Dillon et al (1995) for more details.

The fluid–solid interfaces within the porous media section require special treatment to enforce the prescribed boundary conditions for advection-reaction-diffusion Eqs. (7) and (8). The model requires Neumann (zero-flux) boundary conditions or Dirichlet boundary conditions at these interfaces. The type of boundary condition on each particle can be set independently, and may be dependent on the chemical species as well. Because we prescribe the boundary conditions at the interfaces, we do not need to solve the advection-reaction-diffusion equations in the interior of the particles. Within the fluid phase, we use a standard five-point stencil for the discretized Laplacian ∇^2. We call a grid point irregular if at least one of the other grid points appearing in its usual five-point stencil is located within a solid particle. Several initialization subroutines have been developed to identify the irregular grid points within the fluid phase.

Because the time steps for the fluid solver are small, we can use an explicit method for solving the advection-reaction-diffusion system. At irregular grid points, we make use of the boundary condition to develop an equation for the Laplacian approximation. For both types of boundary conditions Neuman or Dirichlet, we use methods similar to those described by Morton and Mayers (1994). At irregular points near a Dirichlet boundary, the grid point in the interior of the solid particle is replaced by the point lying on the intersection of the grid line and the particle boundary. The concentration at this point is known. The central-difference operator is modified to reflect the fact that the distance γ between the irregular grid point and the particle boundary along the mesh line is less than the mesh width Δx. This can create problems of numerical instability in an explicit method because the size of the time step is constrained by the size of the mesh width. To guarantee numerical stability, we constrain γ so that $\gamma/\Delta x > \epsilon$ where $\epsilon \approx 0.1$.

For Neumann boundary conditions, we use the prescribed Neumann boundary data to replace the missing stencil points in the discretized Laplacian operator. This approach requires an approximation to the normal derivative to the boundary. This information can be readily obtained from the boundary configuration. The discretization to the second derivatives is of lower order than the standard discretization using central differences at regular grid points, and computes solutions that are only first-order accurate in space rather than second order. However, the immersed boundary method generally yields only first-order accuracy in space near the boundaries and so the methods used here are compatible. Nevertheless, in future work we intend to strengthen the numerical implementation of the model by incorporating a higher-order method for the chemical solver.

CONVERGENCE STUDIES

Previous convergence studies of the immersed boundary method have indicated that the method is first-order convergent in space (Peskin and McQueen, 1989a; Roma, 1996). A convergence study for the microchannel version of this model was presented in Dillon et al. (1996). In that study, the convergence was shown to be first order in space for the fluid velocities and locations of the swimming bacterial cells. Our goal here is to demonstrate convergence in a representative porous media simulation. There are a number of aspects of the calculations which might complicate convergence. These include the random aspect of the cell-swimming directions, and the all-or-nothing decisions made in breaking or forming cell–cell or cell-particle links. Nevertheless, we have evidence of first-order spatial convergence, consistent with previous studies. We also show first-order spatial convergence for the solutions to the advection-diffusion-reaction equations.

We performed several numerical experiments on 64×64, 128×128, 256×256, 512×512 grids. The dimensions of the fluid domain was 80 μm $\times$ 80 μm. Our test runs included 8 solid particles approximately 15 μm in diameter, and 12 discrete microbial cells approximately 1.5 μm in diameter. Unattached bacterial cells were motile and chemotactic. The swimming forces produced bacterial swimming speeds of approximately 10 μm s^{-1} in an open microchannel as in Dillon et al. (1996). Attached bacterial cells were nonmotile. In these test runs, a Dirichlet boundary condition for a single chemical was imposed at one of the solid particle/fluid interfaces. This boundary condition fixed the dimensionless concentration at one on the boundary. At each of the other solid particle/fluid interfaces, a zero-flux or Neumann boundary condition was imposed. Periodic boundary conditions for the fluid and chemical were imposed at the edges of the square computational domain. Initially, the chemical concentration was zero throughout the domain except within the saturated particle where the concentration was one. The fluid, initially at rest, was driven by a uniform-pressure gradient (left to right). The bacterial consumption rate for Eq. (7) was of the form

$$R_s(s,a) = -\alpha s(\mathbf{x},t) \quad (10)$$

with consumption rate constant $\alpha = 0.01$ s^{-1}. For comparison purposes, we used the same time step on each grid ($\Delta t = 0.625 \times 10^{-6}$ s)). This step was small enough to avoid numerical instabilities on the finest grid. Note that the number of immersed boundary points around a bacterial cell ring increased from 6 on the coarsest grid to 48 on the finest. The

number of immersed boundary points around a solid particle increased from 77 on the coarsest grid to 616 on the finest.

In Figure 3 we present qualitative evidence of convergence by looking at snapshots of the porous media domain, cells and fluid velocity field at the same time for the 64 × 64, 256 × 256 and 512 × 512 grids. For clarity, the graphs display only a 32 × 32 velocity field. Note that we have depicted the nominal locations of the cell and particle boundaries. The effective size of these particles is actually larger because their forces are spread to the fluid grid beyond the immersed boundary. This is due to the approximate delta function described in the previous section. As the grid is refined, the effective size of the particles tends to the nominal size. In addition, as the grid is refined, the effective porosity of the porous media section increases because the effective size of the particles decreases. Because of this, the fluid velocities increase. This can be seen in Figure 3a–c by examining the flow between the pair of solid particles in the lower right quadrant. In this region, the fluid speeds, as indicated by the length of the vectors, is lower on the coarsest grid (Fig. 3a). As noted above, the number of immersed boundary points in the bacterial cells and solid particles increase as the grid is refined. As a result, the boundaries of these objects become smoother and less polygonal as the grid is refined. There is a single elastic link in this simulation. This connects the bacterial cell and solid particle in the upper left quadrant. Because of the discrete nature of the links, the location of the link forces change as the grid is refined. Overall, the solutions on the two finest grids are very similar.

We compare the velocity fields at time $t = 1.25 \times 10^{-3}$s, which corresponds to 2000 time steps. We assume that the error $\|u_N - u\| = C\Delta x^r$, where $N = 64, 128, 256, 512$ and u is the "true" solution. In order to determine the order of convergence rate r, following LeVeque and Li (1997), we examine the ratio:

$$\frac{\|u_{512} - u_{256}\|}{\|u_{512} - u_{128}\|} \approx \frac{Ch^r - C(2h)^r}{Ch^r - C(4h)^r} = \frac{1 - 2^r}{1 - 4^r} \qquad (11)$$

Here, h is the value of the grid-spacing Δx in the 512 × 512 run. We show the convergence rates computed from our data using the above ratio in Table I, using the L_1, L_2, and L_∞ norms. In addition, we show the convergence rates computed from similar ratios where the values of the velocity field on coarser grids are compared to the corresponding values on the 512 × 512 grid (see Table I). The convergence rates in the L_∞ norm are sublinear on the coarsest grids but approach first order as the grid is refined. The low-convergence rate seen on the coarsest grid is due, in part, to the discrete nature of the elastic links. The convergence rates in the L_1 and L_2 norms show first-order convergence. As shown in Table II, the convergence rates for the chemical suggests first-order convergence in all three norms.

We also examined the convergence of maximum fluid speeds obtained on each grid. Table III shows the maximum fluid speeds obtained on each grid and the relative errors with respect to the maximum speed on the finest grid. The convergence ratios 0.128 (A/B) and 0.372 (B/C) correspond to convergence rates r of 2.0 and 1.3, respectively.

COMPUTER SIMULATIONS

In this section we describe numerical results from simulations of the full model. In each of these, we simulate the transport and reaction of fluid, nutrient (s), oxygen (a) and bacterial cells within a two-dimensional microscale model of porous media. The bacterial cells are motile unless attached to another bacterial cell or to a particle surface. Bacteria consume both nutrient and oxygen, and hence, serve as local and possibly mobile chemical sinks. The chemotactic response of the microbes is governed by the nutrient field s. In each of the simulations the fluid domain has dimensions 80 μm × 80 μm and includes 8 cylindrical particles of approximately 15 μm in diameter. Periodic boundary conditions are imposed upon the fluid dynamics. The microbes respect this periodicity—e.g. as one leaves the left side of the computational domain, it is reintroduced on the right. Hence, the number of bacterial cells (12) within the domain is constant in time. An alternative to this was used in Dillon et al. (1996) where bacterial cells were introduced randomly

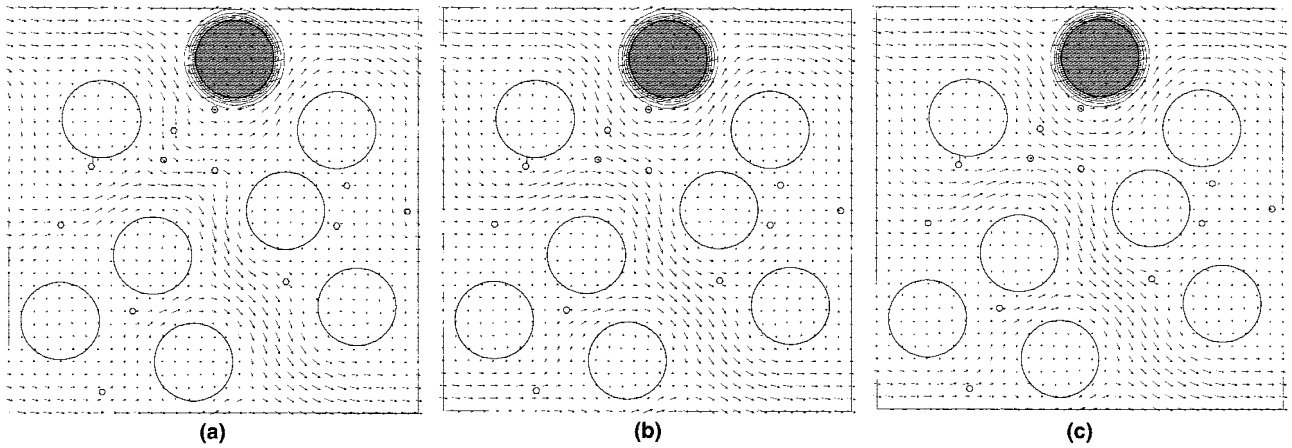

Figure 3. Comparison of fluid and chemical fields. (a) 64 × 64, (b) 256 × 256, (c) 512 × 512. The fluid vector and chemical fields are derived from the common 64 × 64 grid.

Table I. Convergence study of fluid velocity fields.

		L_1	L_2	L_∞
A	$\frac{\|u_{512} - u_{256}\|}{\|u_{512}\|}$	5.79697E-002	5.51803E-002	0.102067
B	$\frac{\|u_{512} - u_{128}\|}{\|u_{512}\|}$	0.172235	0.165180	0.284249
C	$\frac{\|u_{512} - u_{64}\|}{\|u_{512}\|}$	0.393318	0.374915	0.46498
	A/B (r)	0.3366 (.98)	0.3341 (1.0)	0.3591 (.84)
	B/C (r)	0.4379 (.96)	0.4406 (.95)	0.6113 (.23)

at the inflow boundary and removed at the outflow boundary.

Each simulation tracks the evolution of two chemical fields, a nutrient and oxygen. The nutrient is embedded in one or more particles and has periodic boundary conditions on the square computational domain. The oxygen-boundary conditions will be discussed below.

Simulations 1 and 2: Uncoupled Versus Coupled Reaction Kinetics

In Simulation 1, the consumption rates of oxygen and nutrient in Eqs. (7) and (8) are uncoupled:

$$R_s(s,a) = -\alpha s(\mathbf{x},t)$$
$$R_a(s,a) = -\beta a(\mathbf{x},t). \tag{12}$$

These first-order-reaction rates assume that the nutrient and oxygen concentration levels are far from saturated with respect to an underlying Michaelis—Menten consumption rate.

Initially, the fluid velocity field is zero, and the dimensionless concentrations of both the nutrient and oxygen are set equal to one throughout the fluid phase of the domain. The uppermost particle is saturated with nutrient throughout the simulation in the sense that the concentration level of the nutrient is fixed at the particle boundary. Hence, a Dirichlet boundary condition for the nutrient is enforced at this particle boundary. The nutrient is transported by advection and diffusion within the fluid-filled space of the domain. On each of the other particles, a zero-flux Neuman boundary condition is imposed on the nutrient. Thus, the nutrient does not penetrate the other solid particles. Periodic boundary conditions at the four edges of the computational domain are also imposed.

Table II. Convergence study of chemical field.

		L_1	L_2	L_∞
A	$\frac{\|u_{512} - u_{256}\|}{\|u_{512}\|}$	7.73452E-004	9.27517E-004	3.58669E-003
B	$\frac{\|u_{512} - u_{128}\|}{\|u_{512}\|}$	2.61467E-003	3.03248E-003	1.38789E-002
C	$\frac{\|u_{512} - u_{64}\|}{\|u_{512}\|}$	7.90867E-003	8.89246E-003	3.34088E-002
	A/B (r)	0.2958 (1.25)	0.3058 (1.18)	0.2584 (1.52)
	B/C (r)	0.3306 (1.46)	0.3410 (1.41)	0.4154 (1.06)

Table III. Convergence study of maximum fluid speeds (μm s^{-1}).

Grid	512	256	128	64
Speed	360.6	356.0	324.5	263.6
Relative Error		0.0128 (A)	0.100 (B)	0.269 (C)

In addition, oxygen is continually supplied at the inflow boundary with a dimensionless concentration fixed at one. The flux of oxygen at the outflow boundary on the right is assumed to be due entirely to advective transport with zero diffusive flux. A zero-flux Neuman boundary condition is imposed for oxygen on each of the solid particle boundaries. Periodic boundary conditions are imposed on the top and bottom of the computational domain. In Figure 4 we show a time sequence from this simulation.

In Simulation 2, the reaction kinetics at the bacterial centroids are coupled via the equations:

$$R_s(s,a) = -\alpha s(\mathbf{x},t)a(\mathbf{x},t)$$
$$R_a(s,a) = -\beta s(\mathbf{x},t)a(\mathbf{x},t) \tag{13}$$

In all other respects, the governing equations for Simulation 1 and 2 are identical.

A sequence from this simulation is shown in Figure 5. Initially, the dimensionless concentrations of the nutrient and oxygen are fixed at one throughout the fluid domain. If there were no microbes present to ingest the chemicals, both the nutrient and oxygen concentration levels would remain at one. Note that the consumption rates used in these simulations were chosen to illustrate the capabilities of this model. The rates used are one or two orders of magnitude higher than might be expected for oxygen. Thus, the effect of microbial consumption on the chemical concentrations is exaggerated.

In Simulations 1 and 2, a quasi-steady state for the chemical concentrations is reached. The fluctuations in concentration levels are due to the moving bacterial cells. The gradients of oxygen and nutrient shown in Figure 4, are sharper than the gradients shown in Figure 5. This can be seen by comparing the regions of low oxygen and nutrient concentrations in the two simulations. These areas of these regions are larger in Figure 4. The difference is due to the coupling of the reaction kinetics. Decreasing levels of nutrient and oxygen lead to decreasing consumption rates in both species.

Simulation 3: Coupled Reaction Kinetics—Limited Oxygen

Simulation 3 assumes the same reaction kinetics as Simulation 2, the only difference being in the boundary conditions for oxygen. Here, periodic boundary conditions for oxygen are imposed at all sides of the computational do-

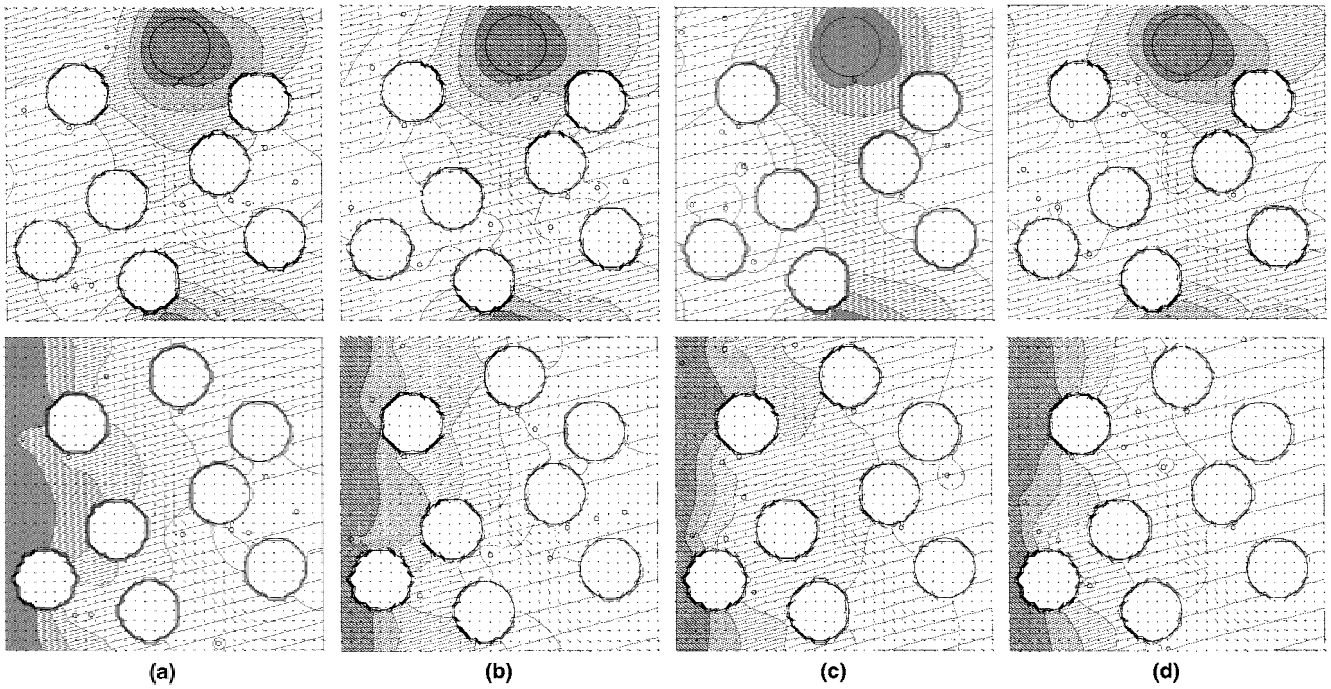

Figure 4. Simulation 1 with uncoupled biochemical reaction of oxygen and nutrient. Top row shows concentration contours for substrate, bottom row for oxygen with fixed-inflow-boundary conditions at times (a) 1.875, (b) 3.75, (c) 5.625, (d) 7.5 seconds. Computational domain for simulation: 64 × 64. Dimensionless concentration of both species ranges from (0,1). Concentration-contours-level lines drawn on concentration levels which are integer multiples of 1/10. $\alpha = \beta = 0.01\ s^{-1}$.

main. A zero-flux boundary condition is imposed on the particle boundaries, as before. In the absence of microbial consumption, these boundary conditions imply a conservation of oxygen within the computational domain. However, as oxygen is consumed, it is not replenished as in Simulation 2. A sequence from this simulation is shown in Figure 6. Note that the total oxygen-concentration level decreases monotonically in time. Because nutrient consumption is proportional to oxygen concentration as shown in Eq. (13), declining levels of oxygen reduce the consumption rate of nutrient. The nutrient level initially decreases, but eventually increases toward the concentration level at the saturated particle boundary.

Simulation 4: Coupled Reaction Kinetics—Motility Dominated

Simulation 4 (Fig. 7) assumes the same reaction kinetics and chemical boundary conditions as Simulation 2. However, the pressure gradient driving the background flow has been reduced by a factor of 100. Because of this, the bacterial cell trajectories are affected more by their own swimming forces and chemotactic responses than the advection by the background flow. In Figure 8b we depict the tracks of the microbes for the duration of the simulation. We are able to see a marked accumulation of the microbes in the region of the uppermost nutrient-saturated particle. In fact, this is more pronounced when one considers the periodic nature of the domain. The cells moving down towards the bottom middle are actually tending towards this particle. Figure 8a shows the corresponding microbe tracks of Simulation 2. These are clearly dominated by the background fluid flow and their spatial distribution over the course of the simulation is more uniform. When one interprets the microbes as moving chemical sinks whose strengths are also dependent upon the concentrations, it is no wonder that the concentration fields in Simulations 2 and 4 are quite different.

Figure 9 shows normalized average-concentration levels of both nutrient and oxygen over the course of each of the simulations as a function of time. In Simulation 1 [panel (a)] the reaction rates are uncoupled. The average-concentration levels of oxygen and nutrient are similar and reach a temporal quasi-steady state after an initial transient. The fluctuations in average-concentration levels is due, in part, to the movement of bacterial cells and hence, consumption sites. In Simulation 2 [panel (b)] the reaction rates are coupled. Decreasing levels of oxygen lead to increasing levels of nutrient, because oxygen as well as nutrient is needed to consume nutrient. This allows the nutrient level to recover somewhat due to the source at the saturated particle. Increased levels of nutrient lead to further decreases in the levels of oxygen. In Simulation 3 [panel (c)] oxygen is not replenished, and its concentration falls exponentially toward zero as the simulation progresses. Initially, the concentration levels of nutrient decrease. However, they reach a minimum, and thereupon increase monotonically toward the concentration level of one. In Simulation 4 [panel (d)], the

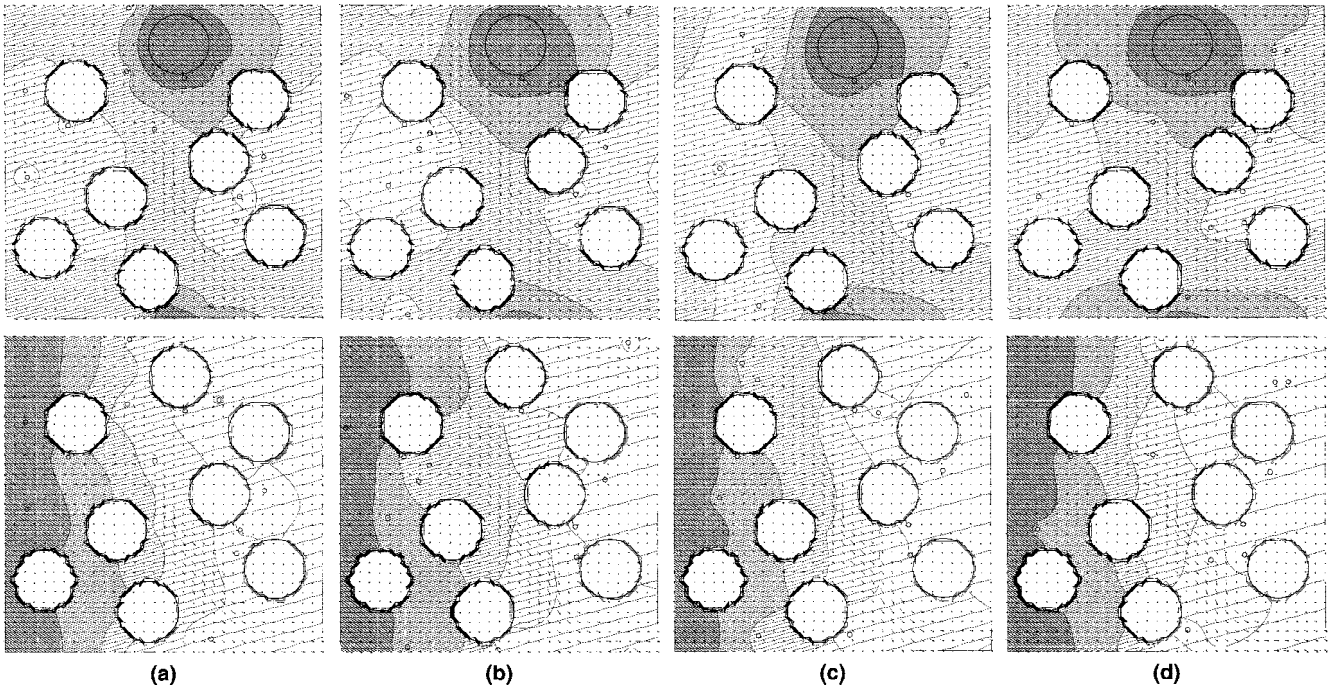

Figure 5. Simulation 2 with fixed-inflow-boundary conditions for oxygen and coupled reaction. Top row shows concentration contours for substrate, bottom row for oxygen at times (a) 1.875, (b) 3.75, (c) 5.625, (d) 7.5 seconds. The numerical grid and concentration contour line levels are the same as in Figure 4.

chemotactic-dominated case as compared to Simulation 2 [panel (b)], the oxygen profiles drop off further and the recovery of the nutrient is more pronounced. This is, in part, due to the microbial sinks being localized closer to the particle that is a nutrient source.

DISCUSSION

We have presented a mathematical model and numerical method that describes the coupled, dynamic, nonlinear interaction of fluid, microbes, and chemical species within

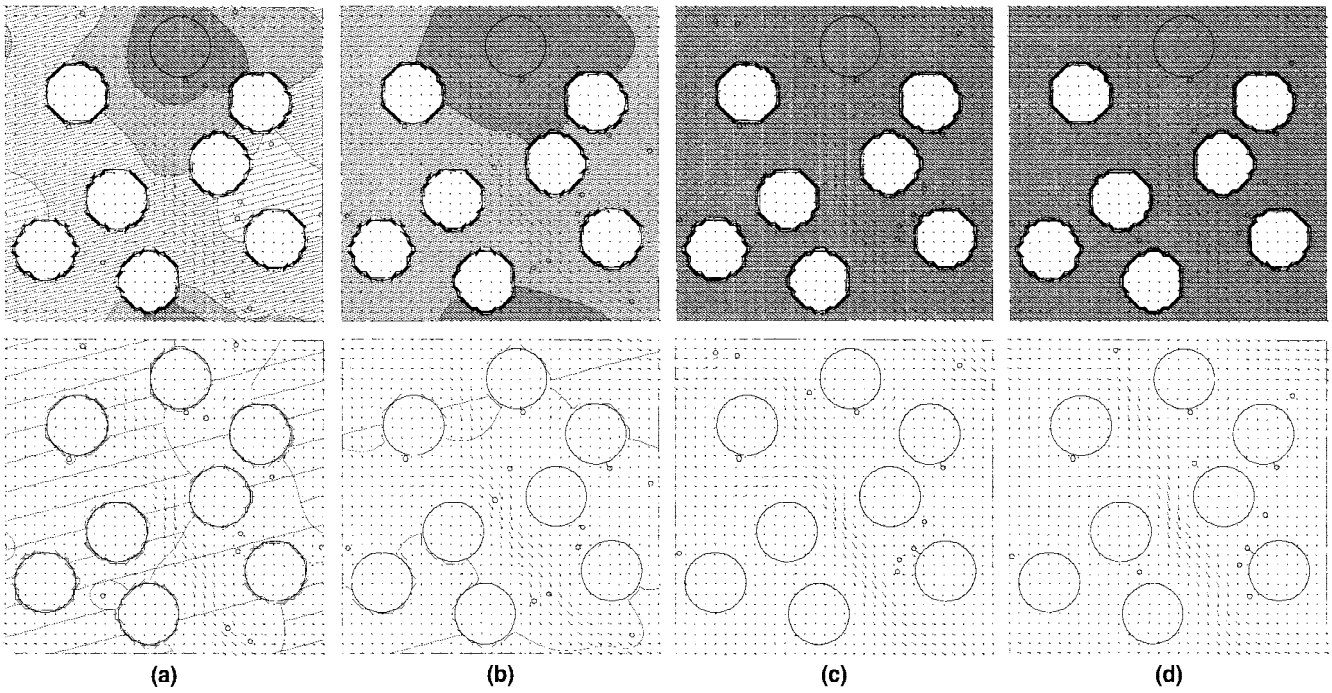

Figure 6. Simulation 3 with periodic boundary conditions for oxygen. Top row shows concentration levels of substrate, bottom row for oxygen at times (a) 1.875, (b) 3.75, (c) 5.625, (d) 7.5 seconds. The numerical grid and concentration contour line levels are the same as in Figure 4.

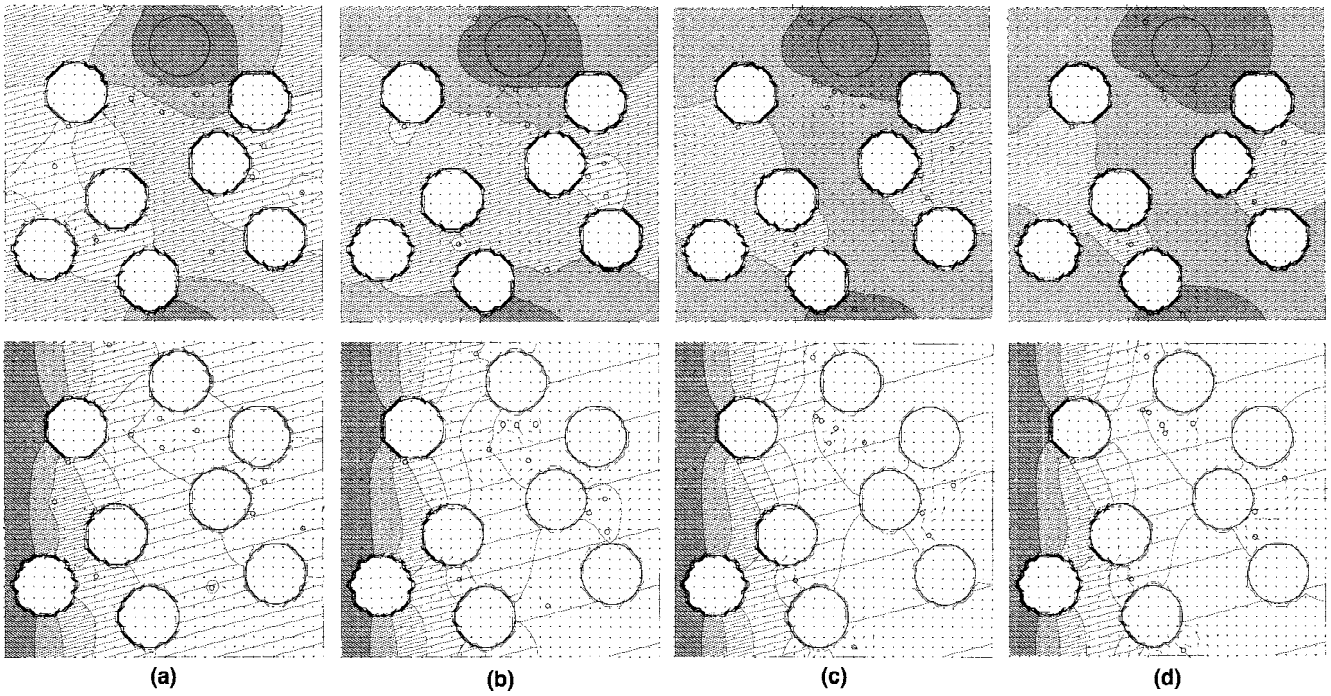

Figure 7. Simulation 4 with coupled biochemical reaction of oxygen and nutrient and reduced background flow. Top row shows concentration contours for a substrate, bottom for oxygen with fixed-inflow-boundary conditions at times (a) 1.875, (b) 3.75, (c) 5.625, (d) 7.5 seconds. The numerical grid and concentration contour line levels are the same as in Figure 4.

porous media. This microscale model includes microbial motility, chemotaxis, and aggregation as well as reaction kinetics and transport of chemicals.

Typical microscale models of porous media represent the solid phase as either a porous matrix in which the matrix is connected in space, or as an assemblage of solid particles. In either case, the fluid mechanics are described by the Stokes or Navier–Stokes equations. In our model it is possible to use either description. In the standard derivations of Darcy's law for porous media, the microstructure is assumed to be periodic on a small-length scale. The coefficients of the Darcy permeability tensor depend upon the details of the microstructure and can be determined by solving a Stokes equation on the microdomain. The microscale fluid equations can be solved using conventional numerical methods such as finite elements or finite differences. The advantage of the immersed boundary method is that it can readily include the movement, attachment, and detachment of bacterial cells within microscale media. These processes are dependent upon the local fluid velocities, and can significantly alter the pore geometry and should be included in a microscale model.

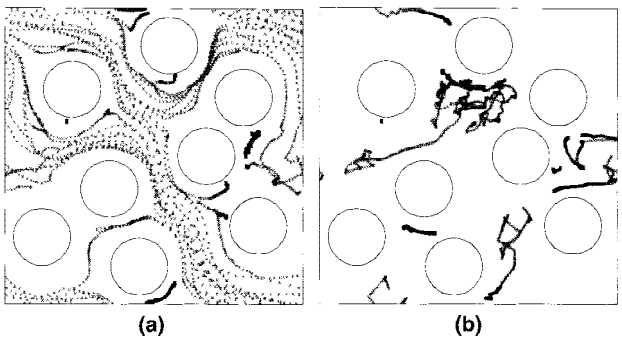

Figure 8. (a) Simulation 2. (b) Simulation 4.

We have set up a controlled environment where we can systematically study the effects of various parameters, including flow rates, reaction rates, microorganism swimming speed, microbial adhesion strengths, boundary conditions for chemicals, and the geometry of the porous media section. For consistency, we examined several different scenarios using a particular microstructure model with an inhomogeneous distribution of substrate-saturated particles. Our simulations showed that the effect of the inhomogeneity depended upon the substrate-reaction kinetics and concentration levels of oxygen. If the kinetics were coupled with oxygen, then substrate-reaction rates dropped in low-oxygen regions. This led to a spatially uniform distribution of high levels of substrate in the bulk fluid due to diffusion and advection. In oxygen-rich regions, substrate-reaction rates were high and the substrate in the bulk fluid was localized to the vicinity of the saturated particles. We also showed that the background flow rates helped to determine the spatial distribution of chemotactic, motile bacteria. In low-flow regimes, we saw accumulation of chemotactic bacteria near the saturated particle, whereas in high-flow regimes, the motile bacteria were more randomly distributed by the advective-dominated transport, and the bacterial chemotactic response was not effective.

Our model is well suited to study the heuristic features of this complex dynamical system. In addition, because we are

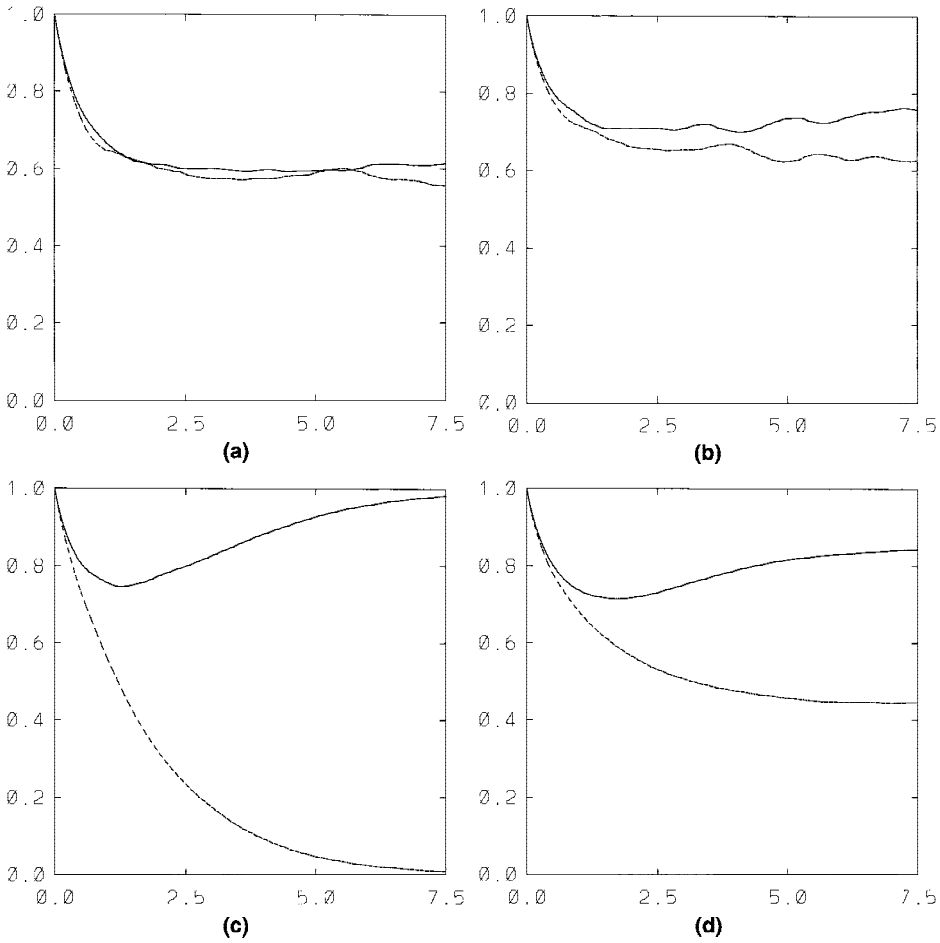

Figure 9. Normalized average-concentration levels for (a) Simulation 1, (b) Simulation 2, (c) Simulation 3, and (d) Simulation 4 over the time interval 0,7.5 s. Nutrient shown by solid line, oxygen by dotted line.

tracking the dynamical evolution of the fluid and chemicals by solving the partial differential equations that govern the physics of the system, the parameters for these processes can be specified and calibrated for particular experiments. The kinetics for the microbial biochemical processes as well as the appropriate swimming and chemotactic characteristics can also be specified and tailored for particular organisms. Of course, bacterial and biofilm dynamics in porous media is a three-dimensional system. Our model is not inherently two-dimensional, and we plan to extend the numerical method to three dimensions in the near future.

The work of R. Dillon was supported by a NSF Postdoctoral Research Fellowship DMS-9508815 and NSF grant DMS-9805501. The work of Lisa Fauci was by NSF grant DMS 9805492 and the NSF Group Infrastructure Grant DMS 9709754.

References

Arthurs KA, Moore LC, Peskin CS, Pittman EB, Layton HE. 1998. Modeling arteriolar flow and mass transport using the immersed boundary method. J Comput Phys 147:402–440.

Baveye P, Valocchi A. 1989. An evaluation of mathematical models of the transport of biologically reacting solutes in saturated soils and aquifers. Wat Resour Res 25:1413–1421.

Bishop PL. 1997. Biofilm structure and kinetics. Wat Sci Tech 36: 287–294.

Chen B, Cunningham A, Ewing R, Peralta R, Visser E. 1994. Two-dimensional modeling of microscale transport and biotransformation in porous media. Numer Meth PDE's 10:65–83.

Chorin AJ. 1968. Numerical solution of the Navier–Stokes equations. Math Comput 22:745–762.

Dillon R, Othmer HG. 1999. A mathematical model for outgrowth and spatial patterning of the vertebrate limb bud. J Theor Biol 197: 295–330.

Dillon R, Fauci L, Gaver D. 1995. A microscale model of bacterial swimming, chemotaxis and substrate transport. J Theor Biol 177:325–340.

Dillon R, Fauci L, Fogelson A, Gaver D. 1996. Modeling biofilm processes using the immersed boundary method. J Comput Phys 129:57–73.

Eggleton CD, Popel AS. 1998. Large deformation of red blood cell ghosts in a simple shear flow. Phys Fluids 10:1834–1845.

Fauci LJ, Fogelson AL. 1993. Truncated Newton methods and the modeling of complex immersed elastic structures. Comm Pure Appl Math 46:787–818.

Fauci LJ, Peskin CS. 1988. A computational model of aquatic animal locomotion. J Comput Phys 77:85–108.

Fogelson AL. 1984. A mathematical model and numerical method for

studying platelet adhesion and aggregation during blood clotting. J Comput Phys 56:111–134.

Hermanowicz SW. 1997. A model of two-dimensional biofilm morphology. Wat Sci Technol 37:219–222.

LeVeque RJ, Li Z. 1997. Immersed interface methods for Stokes flow with elastic boundaries or surface tension. SIAM J Sci Comp 18(3): 709–735.

Morton KW, Mayers DF. 1994. Numerical solution of partial differential equations. Cambridge: Cambridge University Press.

Paulsen JE, Oppen E, Bakke R. 1997. Biofilm morphology in porous media, a study with microscopic and image techniques. Wat Sci Tech 36:1–9.

Peskin CS. 1977. Numerical analysis of blood flow in the heart. J Comput Phys 25:220–252.

Peskin CS, McQueen DM. 1989a. A three-dimensional computational model for blood flow in the heart I. Immersed elastic fibers in a viscous incompressible fluid. J Comput Phys 81:372–405.

Peskin CS, McQueen DM. 1989b. A three-dimensional computational model for blood flow in the heart II. J Comput Phys 82:289–297.

Picioreanu C, Van Loosdrecht MCM, Heijnen JJ. 1998. Mathematical modeling of biofilm structure with a hybrid differential-discrete cellular automaton approach. Biotechnol Bioeng 58:101–116.

Roma AM. 1996. A multilevel self adaptive version of the immersed boundary method. Ph.D. thesis, New York University, New York.

Szego S, Cinnella P, Cunningham AB. 1993. Numerical simulation of biofilm processes in closed conduits. J Comput Phys 108:246–263.

Tebes-Stevens C, Valocchi AJ, VanBriesen JM, Rittmann BE. 1998. Multicomponent transport with coupled geochemical and microbiological reactions: Model description and example simulations. J Hydrol 209: 8–26.

Wimpenny JWT, Colasanti R. 1997. A unifying hypothesis for the structure of microbial biofilms based on cellular automaton models. FEMS Microbiol Ecol 22:1–16.